Journal of Power Sources 193 (2009) 944–949

Contents lists available at ScienceDirect

Journal of Power Sources

journal homepage: www.elsevier.com/locate/jpowsour

Wide-temperature range operation supercapacitors from nanostructured activated carbon fabric

Kaihsuan Hung[a], Charan Masarapu[b], Tsehao Ko[a], Bingqing Wei[c,*]

[a] Department of Materials Science, Feng Chia University, Taichung 40724, Taiwan
[b] Department of Electrical Engineering, University of Delaware, Newark, DE 19716, USA
[c] Department of Mechanical Engineering, University of Delaware, Newark, DE 19716, USA

ARTICLE INFO

Article history:
Received 22 December 2008
Received in revised form 17 January 2009
Accepted 28 January 2009
Available online 7 February 2009

Keywords:
Supercapacitor
Activated carbon fabric
Organic electrolyte
Temperature effect

ABSTRACT

Electrochemical power sources that offer high energy and power densities and, can also withstand a harsh temperature range have become extremely desirable in applications ranging from civilian portable electronic devices to military weapons. In this report, we demonstrated a wide temperature withstanding supercapacitor which can be operated from 100 °C to −40 °C within a voltage window from −2 V to 2 V. The performance of the supercapacitor coin cells, assembled with nanostructured activated carbon fabric (ACF) as the electrode material and 1 M tetraethylammonium tetrafluoroborate ($TEABF_4$) in polypropylene carbonate (PC) solution as the electrolyte, was systematically studied within the set temperature window. The ACF supercapacitor yielded ideal rectangular shapes in cyclic voltammograms within 0–100 °C with an average mass capacitance of 90 F g^{-1} and, 60 F g^{-1} at −25 °C. The capacitance was still over 20 F g^{-1} at the extremely low temperature of −40 °C. Another exciting feature of the ACF supercapacitors was that they resumed their room temperature capacitance when cooled from 100 °C and defrosted from −40 °C, demonstrating an excellent repeatability and stability. The charge–discharge behavior of the ACF supercapacitors showed long-cycle stability at extreme temperatures. These high electrochemical performances make this type of supercapacitors very promising in many practical applications.

1. Introduction

Electrochemical supercapacitors, which deliver 100 times the power of batteries and store 10,000 times more energy than conventional capacitors, are now under urgent scrutiny for widely possible uses in power electronics for back-up memories and peak power saving [1–3]. Therefore, supercapacitors that can withstand a harsh temperature range have become extremely desirable in many applications such as hybrid electric vehicles, portable electronic devices and as aerospace power sources. At present, commercially available non-aqueous supercapacitors are rated for a maximum operating temperature of 85 °C [4]. To the best of our knowledge, however, supercapacitors with organic liquid electrolytes that can be operated at 100 °C or higher have not yet been reported. In this paper, we report our effort to extend the high-temperature operational limit of supercapacitors to 100 °C.

Nanostructured activated carbon fabric (ACF) is one form of activated carbon that is prepared from artificial fibers by an activation process at high temperature [5]. Along with its high specific surface area and uniform pore size distribution with pore diameters less than 2 nm which are crucial for a supercapacitor electrode material, ACF provides additional advantages of flexible fabric configuration, easily being manipulated in terms of shape and size, good conductivity to avoid the usage of current collectors, and the woven feature to avoid the usage of a binder material [6,7]. All of these will significantly increase the energy and power density of the supercapacitors.

An organic electrolyte system has a wider tolerance in both of the potential window and the temperature range compared to an aqueous electrolyte system [8]. Few studies are available in the open literature pertaining to the temperature dependent performance of the organic electrolyte based supercapacitors with activated carbons. Kotz et al. [9] investigated the electrochemical behavior of an activated carbon based supercapacitor using 1 M tetraethyl ammonium tetrafluoroborate ($TEABF_4$) in acetonitrile and in propylene carbonate (PC) electrolytes in the temperature range of −40 °C to 70 °C. Similar temperature dependent measurements have been done on activated carbon supercapacitors by Liu et al. [10]. However, the upper temperature operation were limited to 60 °C or 70 °C [9,10], even though PC based electrolytes have the potential to withstand temperatures much higher than 100 °C before getting decomposed [11,12].

In this report, the electrochemical performance of coin cell supercapacitors assembled with the nanostructured ACF electrodes

* Corresponding author. Tel.: +1 302 831 6438; fax: +1 302 831 3619.
E-mail address: weib@udel.edu (B. Wei).

0378-7753/$ – see front matter © 2009 Elsevier B.V. All rights reserved.
doi:10.1016/j.jpowsour.2009.01.083

and 1 M $TEABF_4$/PC electrolyte was systematically studied in a wide temperature window ranging from −40 °C to 100 °C. To our knowledge, this is the widest temperature range of study ever conducted on a supercapacitor with ACF electrodes in $TEABF_4$/PC electrolyte. In the $TEABF_4$/PC electrolyte system, it is assumed that the cations (TEA^+) attach to the shell of polarized PC solvent molecules as charge-complexes and vice versa for the anions [13]. Electrochemical impedance spectra were extensively analyzed to understand the diffusion behavior and the activation energy of the charge-complexes in the electrolyte at low and high temperatures. Based on this analysis, along with the results from the cyclic voltammograms (CVs) measured at scan rates from 5 mV s^{-1} to 100 mV s^{-1}, the variation in the cell capacitance with temperature and scan rate was clearly understood and explained. A schematic thermal model was also presented to enlighten the diffusion behavior of charge-complexes of $TEABF_4$ in the PC organic electrolyte under diffusion control at different temperatures of operation. The stability of the supercapacitor at high temperature was evaluated by running a long cycle charge–discharge study at 100 °C.

2. Experimental

The nanostructured ACF (Challenge Carbon Technology Co., Taiwan) was prepared by a physical activation from PAN-based staple fabrics at 1000 °C. Using a Micromeritics ASAP2010 system, the Brunauer–Emmett–Teller (BET) surface area was determined by an isothermal nitrogen adsorption at 77 K. The surface morphology of ACF was examined by an atomic force microscopy (AFM) and a scanning electron microscopy (SEM). A 1 M $TEABF_4$ dissolved in battery-graded PC solvent (used as received from Alfa-Aesar) was used as the electrolyte. The supercapacitor was assembled in a coin cell by placing a Wattman glass microfiber filter paper as a separator between two circular ACF electrodes (0.5 in. in diameter) in a glove box under Ar atmosphere with H_2O and O_2 levels less than 0.1 ppm. Before the cell assembly, the ACF electrodes were heated to 120 °C in Ar atmosphere for 2 h to evaporate any trace amount of absorbed moisture. The dry weight of each ACF electrode was 6.6 mg. To perform the high-temperature measurements from 25 °C up to 100 °C, the coin cell was placed in a box-oven (LINBERG/BLUE M) capable of maintaining a very stable set temperature up to one-tenth of a °C. An alcohol based circulating cooling system (PolyScience®) was used to conduct the low temperature measurements from 0 °C to −40 °C.

Cyclic voltammograms were measured using an EG & G Parstat®2273 in the potential window from −2 V to 2 V at different scan rates (5 mV s^{-1}, 10 mV s^{-1}, 20 mV s^{-1}, 40 mV s^{-1}, 60 mV s^{-1}, 80 mV s^{-1}, and 100 mV s^{-1}). The mass capacitance (C_g, F g^{-1}) of a two electrode supercapacitor is generally calculated from an integral area of the voltammogram loop as given by the Eq. (1):

$$C_g\,(\mathrm{F\,g^{-1}}) = 2 \times \left(\frac{A_c + A_d}{2 \times \gamma_s \times \Delta V \times m}\right) \quad (1)$$

where A_c and A_d represent the charge area and the discharge area, γ_s is the scan rate, ΔV is the potential window and m is the average mass of the two electrodes. To acquire the AC impedance spectra at equilibrium open circuit potential (~0 V) of the cell, an alternating potential was used with amplitude of 5 mV in the frequency range from 0.01 MHz to 1 MHz. In general, based on the porous electrode mechanism [2], the mass capacitance C_g is dominated by the imaginary part of Nyquist spectra within a sufficiently low frequency range (diffusion control) and the expression can be written as Eq. (2):

$$C_g\,(\mathrm{F\,g^{-1}}) = \frac{-2}{\omega \times \mathrm{Im}\,(Z) \times m} \quad (2)$$

where ω is the angular frequency.

The galvanostatic charge–discharge studies at different temperatures were carried out using an Arbin battery testing system. Two different constant current densities of 1 A g^{-1} and 100 mA g^{-1} were selected to perform the charge–discharge measurements in the voltage window from −2 V to +2 V and evaluate the energy density (Wh kg^{-1}) and power density (W kg^{-1}) of the supercapacitor under the operating temperatures. The cell stability was evaluated by performing a long cycle charge–discharge study with a constant current density of 1 A g^{-1} at 100 °C for up to 10,000 cycles.

3. Results and discussion

3.1. Surface and microstructural analysis of ACFs

Fig. 1(A) shows an isotherm nitrogen adsorption of the ACF electrode. Considering the Brunauer–Deming–Deming–Teller classification [14], the ACF electrode shows a typical Type I adsorption behavior. The hysteresis loop at the relative pressure of 0.3 indicates that the pore structures have a slit-type feature with a diameter smaller than 15 Å. The amount of adsorption volume shows that the ACF electrode has an excellent BET surface area of 1340 $m^2\,g^{-1}$. The huge surface area generally assists in forming high electrical double layer surfaces and give significant capacitance values. The inset of Fig. 1(A) shows the SEM image of the ACF electrode. The woven feature of the fabric configuration provides optimum diffusion avenues for electrolyte within their geometrical spaces.

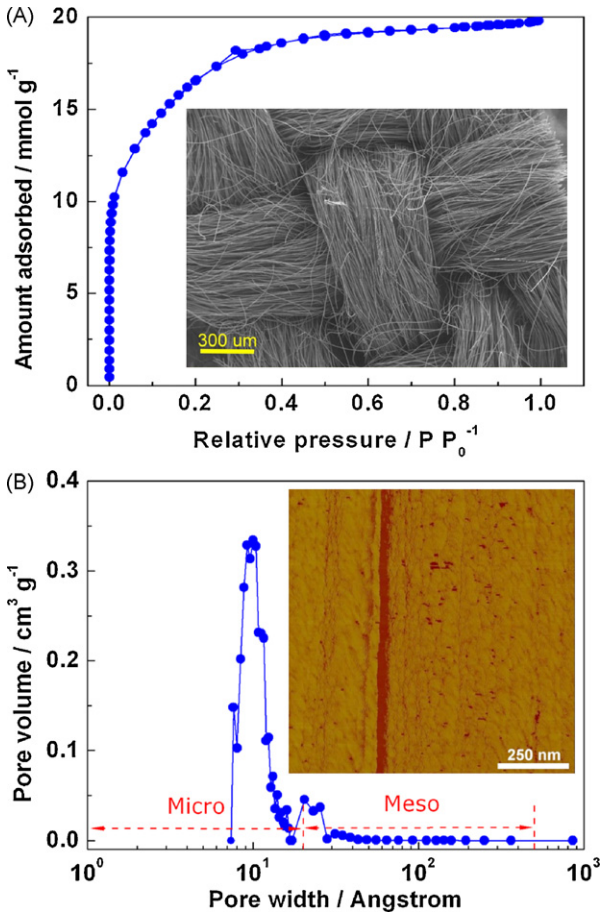

Fig. 1. The surface area and the pore size distribution of ACF. (A) Nitrogen adsorption isotherm with an SEM image inset. The adsorption volume increased sharply below the relative pressures of 0.2 with a small hysteresis loop kneed at 0.3. It then saturated to a plateau at a relative pressure around 0.4 all the way up to 1. (B) Pore size distribution analysis of the ACF electrode: the pore volume versus pore width curve. Inset is an AFM image of the ACF showing its surface morphology.

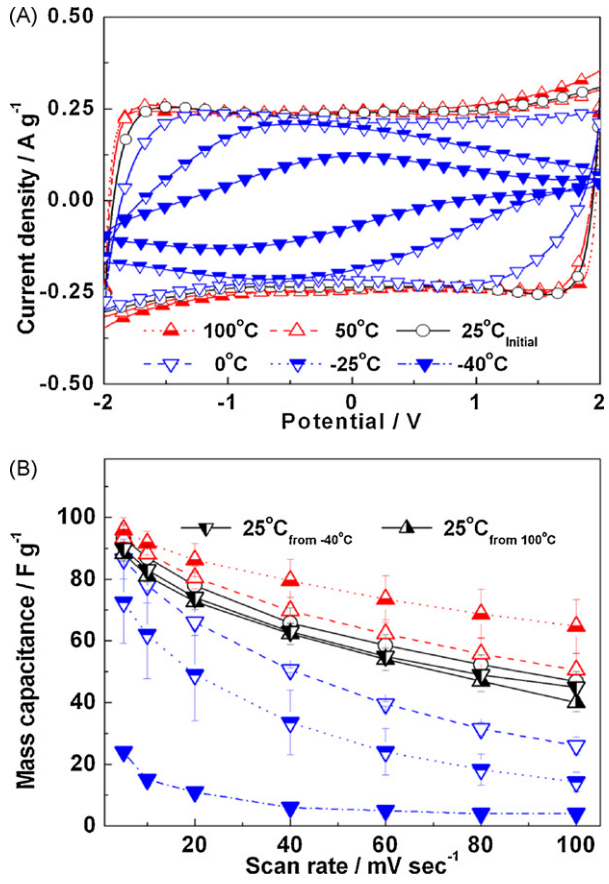

Fig. 2. Potential dynamic performances of ACF electrodes in 1 M $TEABF_4$/PC electrolyte measured as a function of temperature. (A) Cyclic voltammograms measured at different temperatures with the scan rate of 5 mV s^{-1}; (B) mass capacitances (C_g, F g^{-1}) charts at different scan rates and at different temperatures. The value of the capacitance C_g is calculated from the integral surface area of the voltammogram using Eq. (1). The legend used in (A) is the same for (B).

Fig. 1(B) shows the pore size distribution analysis of the ACF electrode via the Barrett–Joiner–Halenda (BJH) method [15]. The pore size is mainly distributed at 10 Å within the micro-pore region and partially at 25 Å within the meso-pore region. The dark holes in the inserted AFM image confirm the micro-pore surface structures. It is estimated that more than 90% of the specific surface area is contributed from the micro-pores with less than 20 Å pore width. The uniform pore size nature of the ACF electrode provides a reliable foundation to investigate diffusion behavior of an electrolyte under the temperature effect.

3.2. Cyclic voltammetry analysis of ACF supercapacitors

Cyclic voltammograms were measured on the assembled ACF supercapacitors at each set temperature from 100 °C to −40 °C with a scan rate from 5 mV s^{-1} to 100 mV s^{-1}. Fig. 2(A) shows the CV curves recorded at different temperatures at the scan rate of 5 mV s^{-1}. The CV curves obtained from 0 °C to 100 °C have rectangular profiles with an ideal capacitive behavior, and represent that the current responds imminently to the scan rate and stay on a saturated plateau. However, the current responses were heavily desaturated at −25 °C and −40 °C and the CV curves deviated from the rectangular behavior, indicating a significant temperature effect on the electrochemical performance of the supercapacitor.

Fig. 2(B) shows the plots of the average C_g value of the supercapacitors calculated from the voltammograms measured at different temperatures versus scan rate. It is not surprising that the C_g value decreases not only by increasing the scan rate, but also by the decrease in the temperature of operation. However, the supercapacitor shows an optimum performance in a very wide temperature window from −25 °C to 100 °C, with a C_g value of 73 F g^{-1} at −25 °C and 96 F g^{-1} at 100 °C at the scan rate of 5 mV s^{-1}, for instance. Even at −40 °C, which is just 9 °C above the melting point of the PC solvent, the supercapacitor still has a reasonably appreciable C_g value of 24 F g^{-1}, which is much higher than the published values obtained at a similar temperature [9].

One important feature of the supercapacitors is their performance retention with repeated heating and cooling cycles, as illustrated in Fig. 2(B). The value of C_g at 25 °C is almost retained every time after cooling back from 100 °C and/or heating back from −40 °C. This is an exciting result and proves that the supercapacitors can be reliably used at any temperatures within −40 °C to 100 °C without losing the cell performance.

3.3. AC impedance analysis of ACF supercapacitors

To understand the fundamentals of the temperature dependence of the electrochemical performance discussed above, the ACF supercapacitors were analyzed using AC impedance. Fig. 3 shows the Nyquist spectra of the supercapacitor measured from 10 kHz to 10 mHz at different temperatures. The Nyquist spectra display an ideal capacitive behavior at each set temperature from 100 °C to −25 °C. However, the ideal feature is lost at −40 °C due to the near frozen PC electrolyte solution. From all the Nyquist spectra, the boundary frequency is noted to be present at approximately 4 Hz. In general, a Nyquist spectrum can be interpreted in the following way. The electrical double layer in the pores of the ACF electrode is constructed by the charge-complexes diffusing towards the Helmholtz plane inside the pores [2,16]. The first intersection

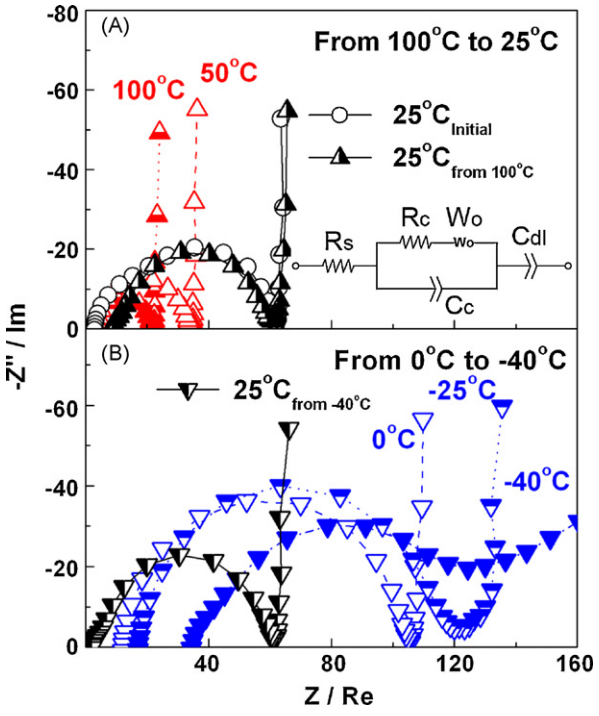

Fig. 3. Nyquist spectra of the ACF supercapacitor as a function of temperature. (A) High-temperature range; (B) low temperature range. The Nyquist spectrum is a complex function of the resistance (R) and capacitance (C) that can correlate the electrochemical behavior of the supercapacitor with an equivalent RC circuit, which is inserted in (A). For an ideal capacitor, the Nyquist spectrum is configured by a semicircle in a high frequency region with a vertical line in a low frequency region. The frequency where the semicircle and the vertical line meet the real axis can be considered as the boundary frequency.

point on the real axis of the Nyquist spectrum in the high frequency region is represented as the bulk solution resistance of the electrolyte (R_s). It then follows a semicircle with a second intersection point on the real axis at medium frequencies. In this region of high frequency to medium frequencies, only small amounts of charge-complexes can overcome the activation energy to migrate with the alternating potential and is called the kinetic control regime. The semicircle is developed by the moving charge-complexes close to the Helmholtz plane and is represented by an interfacial contact capacitance (C_c) and charge transfer resistance (R_c). In the sufficiently low frequency range, the constantly decreasing frequency provides enough time for the charge-complexes present in the diffusion layer to overcome the activation energy and move closer to the Helmholtz plane. These charge-complexes ultimately occupy all the available surfaces inside the micro-pores of the ACF electrodes and contribute to the electrical double layer capacitance (C_{dl}). The low frequency range where C_{dl} is contributed is called the diffusion control regime.

All the circuit elements pertaining to the Nyquist plot can be arranged to form an equivalent circuit as shown in the inset of Fig. 3(A). It is used to fit the Nyquist spectra measured for the supercapacitor at different temperatures. The equivalent circuit is a modified version reported by Wang and Teng [7], where the interfacial contact capacitance C_c and the electrical double layer capacitance C_{dl} are replaced by constant phase elements in order to compensate for the depressed semicircle in the kinetic control and to suitably fit the vertical line in the diffusion control [2]. The diffusion resistance, which can be interpreted using the Warburg diffusion element (W_o) in the diffusion control regime, is another crucial factor to influence the performance of C_g in the equivalent circuit. The equivalent circuit fitting results of the supercapacitor from 100 °C to −40 °C are listed in Table 1. In the kinetic control regime, the bulk solution resistance of the electrolyte R_s and the charge transfer resistance R_c showed a gradual decrease with temperature increase. However, the value of C_c is in the range of few mF g^{-1} and shows much less variation with temperature changes. This is due to the fact that inside the micro-pores, the polarized PC molecules have already occupied the Helmholtz plane due to the smaller size compared to the charge-complexes [13]. When the frequency is high, only limited amount of the charge-complexes will tend to occupy the pores, resulting in a low value of C_c. In the diffusion control regime the Warburg resistance W_o showed a continuous increase with temperature decrease, 2.8 Ω at 100 °C to almost 480 Ω at −40 °C. Consequently the double layer capacitance C_{dl} decreased from 90 F g^{-1} at 100 °C to 36 F g^{-1} at −40 °C. The comparable values of C_{dl} from the fitting data to the values of C_g of the supercapacitor from Fig. 2(B) indicate that the entire mass capacitance C_g of the supercapacitor is predominated by C_{dl} in the diffusion control regime.

The temperature dependence of the diffusion resistance W_o and the charge transfer resistance R_c of the electrolyte can be interpreted and better understood in terms of the activation energy E following an Arrhenius-type Eq. (3):

$$R_o\,(\Omega) = R_{o,0}\exp\left(\frac{E}{kT}\right) \tag{3}$$

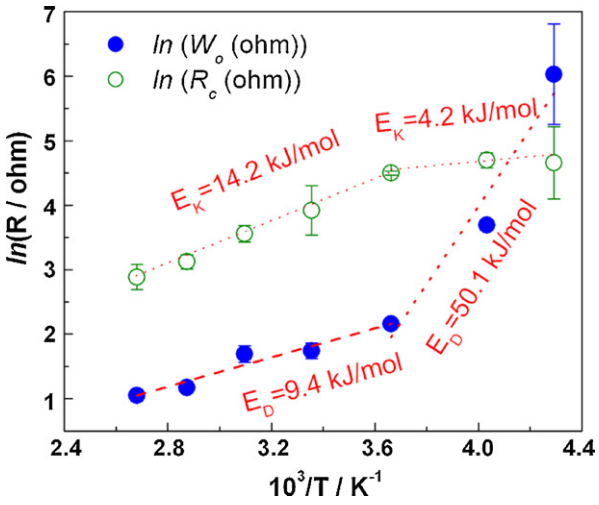

Fig. 4. An Arrhenius plot of the temperature-dependence of diffusion resistances in 1 M $TEABF_4$/PC electrolyte. The mean diffusion resistances were estimated from fitting results of Fig. 3.

where $R_{o,0}$ is a constant, k is the Boltzmann's constant, T is the absolute temperature. Replacing R_o by the values of R_c in Table 1 and by plotting ln(R_c) versus 1/T, the activation energy E_K of the charge-complexes in the electrolyte, to overcome the charge transfer resistance R_c in the kinetic control regime, can be obtained from the slope of the line as shown in Fig. 4. The high (100–0 °C) and low (0 °C to −40 °C) temperature regions of operation can be clearly distinguished from the plot with lines having different slopes in each regions. Similarly, by plotting ln(W_o) versus 1/T, the activation energy E_D of the charge-complexes to overcome the diffusion resistance in the diffusion control regime can be calculated (Fig. 4). It is noted that E_K and E_D have comparable values in the high-temperature region (14 kJ mol^{-1} and 9.4 kJ mol^{-1}, respectively), unveiling a similar temperature effect on both resistances. In the low temperature region, however, E_K (4.2 kJ mol^{-1}) is much less than E_D (50.1 kJ mol^{-1}), indicating that the diffusion resistance is enormously affected by the operation temperature.

Three kinds of variations of C_g can be observed from Fig. 2(B): (i) the decrease in the value of C_g with the increase in the scan rate; (ii) the increase in the value of C_g with the increase in the temperature; and (iii) the variation of C_g at high scan rate of 100 mV s^{-1} is higher than that at low scan rate of 5 mV s^{-1} in the high-temperature region from 0 °C to 100 °C. On the contrary, in the low temperature region from 0 °C to −40 °C, the variation of C_g at high scan rate of 100 mV s^{-1} is lower than that at low scan rate of 5 mV s^{-1}. The variation of the mass capacitance C_g of the supercapacitor with temperature and scan rate can be understood and easily explained based on the activation energy of the charge-complexes in the kinetic and diffusion control regimes and from the fitting results of the impedance spectra (Table 1).

(i) C_g decreases when the scan rate increases. Generally, the charge-complexes TEA^+/PC in the electrolyte have to overcome two resistances. The first resistance comes from the charge-complexes transferring through the pores of the ACF electrode. This resis-

Table 1
The equivalent circuit fitting results of resistances and capacitances from Nyquist spectra shown in Fig. 3.

	100 °C	50 °C	25 °C	0 °C	−25 °C	−40 °C
R_s (Ω)	6 ± 3.4	5 ± 1.3	9 ± 4.8	10 ± 3.3	13 ± 3.4	41 ± 14.6
R_c (Ω)	18 ± 3.3	35 ± 4.2	53 ± 18.2	90 ± 2.8	110 ± 12.8	114 ± 60.8
C_c (mF g^{-1})	2.8 ± 0.5	1.8 ± 0.5	2.5 ± 0.1	1.5 ± 0.1	2.5 ± 0.3	6 ± 3.5
W_o (Ω)	2.9 ± 0.2	5.5 ± 0.7	5.7 ± 0.7	8.7 ± 0.5	40 ± 0	480 ± 339
C_{dl} (F g^{-1})	90 ± 10	85 ± 8	84 ± 9	76 ± 15	75 ± 9	36 ± 21

tance is electrode specific. The variation of this resistance can be attributed to the variation of the charge transfer resistance R_c in the equivalent circuit model. It changes less with the scan rate variation during the CV measurements but varies much with the temperature changes. The other diffusion resistance arises from the migration friction between the charge-complexes and the PC molecules. The migration friction depends on both the scan rate and temperature. To move with a higher velocity in compliance with a high scan rate, the charge-complexes encounter a greater migration friction and sacrifice more kinetic energy to overcome the friction. This phenomenon reduces C_g of the supercapacitor with increase in the scan rate at a particular temperature as seen in Fig. 2(B).

(ii) C_g increases when temperature increases. This phenomenon can be readily presented through the schematic representation in Fig. 5. Fig. 5 (left side) illustrates a schematic model of the electrical double layer constructed in the diffusion control regime at 0.05 Hz near one of the electrodes of the supercapacitor at temperatures of 100 °C, 0 °C and −40 °C. The plots of the mass capacitance calculated from impedance spectra at corresponding temperatures versus frequency are placed adjacent to the schematic in Fig. 5 (right side).

At any particular scan rate, higher kinetic energy obtained from a higher temperature (for instance, 100 °C) enlarges the free spaces in between the charge-complexes and the PC molecules. The migration friction between the charge-complexes and polarized PC molecules is lowered and greatly reduces the diffusion resistance. Under an applied potential, high number of the charge-complexes from the diffusion layer of the electrolyte system will now be able to migrate to the outer Helmholtz plane as in the schematic (top panel) in Fig. 5 and a high value of C_{dl} is observed as shown in Table 1. It has been verified that C_g is predominated by C_{dl} and so a high value of capacitance is observed at 100 °C in Fig. 2(B) at any scan rate. As the temperature is reduced to 0 °C, the kinetic energy is decreased and the polarized PC molecules moves closer to each other. It becomes difficult for the charge-complexes to move to the Helmholtz plane due to the increased migration friction (middle panel). This leads to an increase in the diffusion resistance and a decrease in C_{dl} value (see Table 1). At −40 °C, which is just 9 °C above the melting point of the PC solvent, all the polarized PC molecules become almost tightly packed and give enormous resistance to the charge-complexes to move towards the Helmholtz layer (bottom panel). The value of C_{dl} drastically reduces due to a huge increase in the diffusion resistance as shown in Table 1. This is also evident from the reduction in the mass capacitance C_g from a value of around 96 F g^{-1} at 100 °C to 10 F g^{-1} at −40 °C at 0.05 Hz in Fig. 5 (right side). Thus, the increase in temperature shows a significant improvement in the C_g value at each scan rate, as seen in Fig. 2(B).

(iii) Variation of C_g is affected differently by the scan rate in different temperature regions. The third kind of variation in C_g that is observed in Fig. 2(B) can be divided into two regions. In the high-temperature region (0–100 °C), the migration friction is low at a low scan rate (at 5 mV s^{-1}), all the charge-complexes reach the Helmholtz plane attaining a saturation and yields a high C_g value (Fig. 2(B)). Though the migration friction increases and hinders the movement of charge-complexes at 0 °C, the low scan rate still provides sufficiently enough time for the charge-complexes to move to the Helmholtz plane and therefore, the decrease in the capacitance is not significant at the low scan rate with the temperature decrease (96 F g^{-1} at 100 °C to 87 F g^{-1} at 0 °C). At the high scan rate of 100 mV s^{-1}, however, the high velocity requirement for the movement of the charge-complexes encounters a higher migration friction and therefore a high diffusion resistance, in particular at near 0 °C. So, the decrease in the capacitance is significant at the high scan rate with the temperature decrease (65 F g^{-1} at 100 °C to 26 F g^{-1} at 0 °C).

In the low temperature region (0 °C to −40 °C), in particularly near −40 °C the activation energy required to overcome the diffusion resistance of the tightly packed electrolyte molecules and charge-complexes is so high (Fig. 4) that the charge-complexes can never reach the Helmholtz plane even at the slow scan rate of 5 mV s^{-1}. So a huge decrease in the capacitance is observed at a low scan rate when the temperature is decreased from 0 °C to −40 °C (Fig. 2 (B)). Whatever a small capacitance showed at −40 °C will be mostly from the already existing charge-complexes very close to the inner Helmholtz plane near the pores of the ACF electrode. It is particularly true at the high scan rate (100 mV s^{-1}), where the contribution from the charge-complexes accumulated near the outer Helmholtz plane will be completely negligible but the charge-complexes present in the inner Helmholtz plane remains almost the same as before. Thus, the variation of C_g is significantly larger at the low scan rate of 5 mV s^{-1} (87 F g^{-1} at 0 °C to 24 F g^{-1} at −40 °C) than that at the high scan rate of 100 mV s^{-1} (26 F g^{-1} at 0 °C to 4 F g^{-1} at −40 °C).

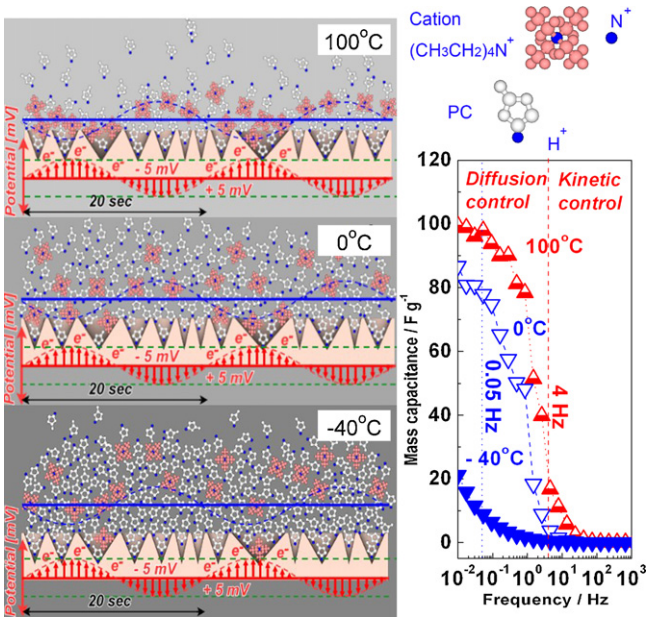

Fig. 5. Schematic diagrams of electrical double layer at temperatures simulated the mass capacitance (F g^{-1}) from AC impedances via Eqs. (2) and (3). In the schematic (right side), the pink color wedges represent the pores of the ACF electrode. The grey color on the top of the wedges is the electrolyte with the polarized PC molecules (represented as PC) and charge-complexes. The sinusoidal wave (red dotted line) under the ACF electrode is the alternating current with amplitude of 10 mV peak–peak and a frequency of 0.05 Hz. This creates a symmetric alternating potential field with a frequency of 0.05 Hz in the electrolyte (blue dotted line). The solid blue line on top of the ACF electrode can be assumed as the outer Helmholtz layer and the space just above the pores of the ACF electrode along the wedges is assumed to be the inner Helmholtz plane. The red dotted line marked at the frequency of 4 Hz in the left plot is the boundary between the kinetic control and diffusion control regimes as noted from the impedance spectra. (For interpretation of the references to color in this figure legend, the reader is referred to the web version of the article.)

3.4. The ragone charts and cell stability of ACF supercapacitors

Fig. 6(A) shows the Ragone chart with the plots calculated from the discharge data of the galvanostatic charge–discharge curves measured at constant current densities 100 mA g^{-1}, 1 A g^{-1} and 10 A g^{-1}. No significant change in the power density and energy density was observed when the cell was discharged with current density of 100 mA g^{-1} at three selected temperatures, 100 °C, 25 °C and −25 °C. From the 100 mA g^{-1} plots, an energy density of around 23 Wh kg^{-1} and a power density of 50 W kg^{-1} were obtained. Increasing the current density to 10 A g^{-1}, the energy density significantly decreased for the discharge data measured

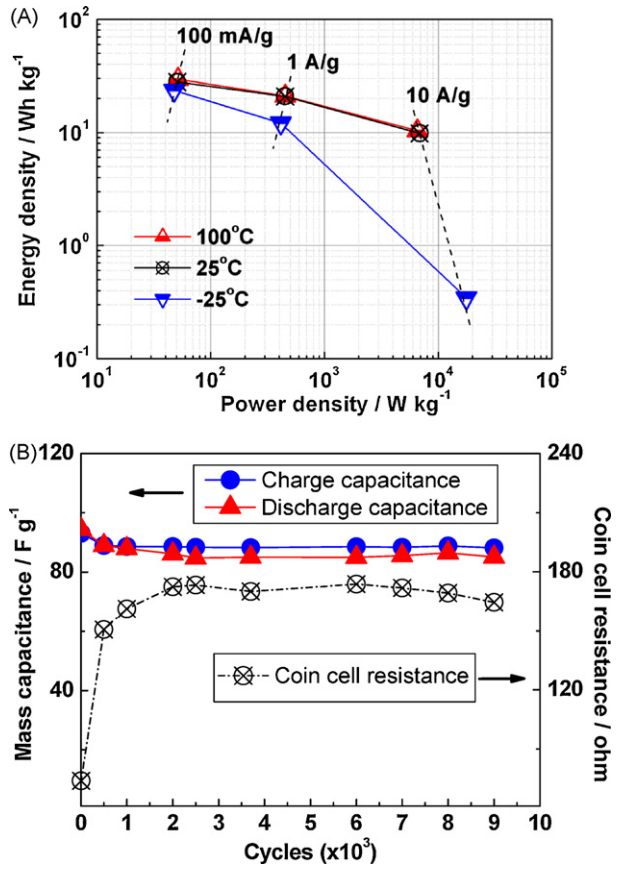

Fig. 6. Ragone plots (A) and cycleability (B) of the ACF supercapacitors. To estimate the energy and power density of the ACF supercapacitor, charge–discharge cycling at three constant current densities of 100 mA g^{-1}, 1 A g^{-1} and 10 A g^{-1} was performed in the voltage window from −2 V to +2 V at temperatures 100 °C, 25 °C and −25 °C. To test the stable performance of the cell at 100 °C, a long cycle charge–discharge measurement at a constant current density of 1 A g^{-1} was carried out up to 10,000 cycles.

at −25 °C compared to the data measured at 100 °C and 25 °C. An energy density of around 15 Wh kg^{-1} and a power density of 7000 W kg^{-1} was obtained from the discharge curve measured with the constant current density of 10 A g^{-1} at 100 °C.

Fig. 6(B) displays the long cycle charge–discharge performance of the cell at 100 °C and the variation of the cell resistance during the cycling calculated from the IR drop present in the discharge curves. The capacitance showed an initial decay of about 20 F g^{-1} in the first 3000 cycles, and stabilized at a constant value of 64 F g^{-1} for the remaining 7000 cycles, demonstrating an excellent long-cycling stability as well as a high specific capacitance of the supercapacitor cell. The behavior of the cell resistance reflected according to the variation of the capacitance, with a value of 73 Ω in the initial cycle, it increased to around 170 Ω during the first 3000 cycles and stayed almost constant at that value during the remaining 7000 cycles of charge–discharge. The charge–discharge cycles on the coin cell was continuously measured in a box-oven for almost two months at 100 °C to finish this experiment, demonstrating the stable operation of the cell at a high temperature of 100 °C. These high electrochemical performances can now make this type of supercapacitors very promising and suitable for high-temperature applications (up to 100 °C).

4. Conclusions

In conclusion, the electrochemical performance of coin cell supercapacitors assembled with nanostructured ACF electrodes using 1 M $TEABF_4$/PC electrolyte was systematically studied in a wide temperature window ranging from −40 °C to 100 °C. To our best knowledge, this is the widest temperature range of study ever conducted on a supercapacitor with ACF electrodes in a $TEABF_4$/PC electrolyte system. Electrochemical impedance spectra were extensively investigated and analyzed to understand the diffusion behavior and the activation energy of the charge-complexes in the electrolyte at low and high temperatures. A schematic thermal model was presented to enlighten the diffusion behavior of the charge-complexes under diffusion control at different temperatures of operation. The variation in the cell capacitance with temperature and scan rate was clearly explained based on these analysis and the cyclic voltammogram results. The nanostructured ACF electrodes with the uniform slit-type micro-pores and a high specific surface area have provided a reasonably appreciable capacitance at the extremely low temperature. The excellent long cycle charge–discharge stability and the thermal repeatability have proved the supercapacitor cells for suitable applications in civilian, military and aerospace which require high energy and power density power sources and harsh temperature operations.

Acknowledgments

This work was financially supported by National Science Foundation (NSF CMMI # 0753462 and 0824790).

References

[1] T. Morimoto, K. Hiratsuka, Y. Sanada, K. Kurihara, J. Power Sources 60 (1996) 239–247.
[2] R. Kotz, M. Carlen, Electrochim. Acta 45 (2000) 2483–2498.
[3] B.E. Conway, J. Electrochem. Soc. 138 (1991) 1539–1548.
[4] http://www.cap-xx.com/product/products.htm.
[5] T.H. Ko, P. Chiranairadul, C.K. Lu, C.H. Lin, Carbon 30 (1991) 647–655.
[6] A.G. Pandolfo, A.F. Hollenkamp, J. Power Sources 157 (2006) 11–27.
[7] K.P. Wang, H.S. Teng, J. Electrochem. Soc. 154 (2007) A993–A2998.
[8] M. Ue, K. Ida, S. Mori, J. Electrochem. Soc. 141 (1994) 2989–2996.
[9] R. Kotz, M. Hahn, R. Gallay, J. Power Sources 154 (2006) 550–555.
[10] P. Liu, M. Verbrugge, S. Soukiazian, J. Power Sources 156 (2006) 712–718.
[11] R. Jasinski, S. Carroll, J. Electrochem. Soc. 117 (1970) 218–219.
[12] X.H. Li, Y.Z. Meng, Q. Zhu, S.C. Tjong, Polym. Degrad. Stab. 81 (2003) 157–165.
[13] J. Chmiola, G. Yushin, Y. Gogotsi, C. Portet, P. Simon, P.L. Taberna, Science 313 (2006) 1760–1763.
[14] S. Brunauer, L.S. Deming, W.S. Deming, E. Teller, J. Am. Chem. Soc. 62 (1940) 1732–1746.
[15] E.P. Barrett, L.G. Joiner, P.H. Halenda, J. Am. Chem. Soc. 73 (1951) 373–380.
[16] H. Shi, Electrochim. Acta 41 (1996) 1633–1639.